



# Catalytic performance of different carbon materials for hydrogen production in sulfur–iodine thermochemical cycle

Yanwei Zhang\*, Rui Wang, Xiangdong Lin, Zhihua Wang, Jianzhong Liu, Junhu Zhou, Kefa Cen

State Key Laboratory of Clean Energy Utilization, Zhejiang University, Hangzhou 310027, China

## ARTICLE INFO

### Article history:

Received 20 August 2014

Received in revised form 26 October 2014

Accepted 13 November 2014

Available online 3 December 2014

### Keywords:

Sulfur–iodine cycle

HI decomposition

Catalytic activity

Carbon materials

Hydrogen production

## ABSTRACT

This study examines four carbon materials through a series of characterization methods and a hydrogen iodide (HI) decomposition test. Applying a traditional structure to carbon materials facilitates the quantitative analysis of the four samples. The X-ray diffraction and Raman spectroscopy results indicate that lesser stacked graphite-like layers and shorter lateral diameter  $L_a$  result in higher disordering structure. However, the quantity of active sites is not determined only by the degree of disordering. The aliphatic carbon in the inter-layer correlations decreases the amount of graphite carbon and occupies its edge, thereby inhibiting the formation of edge sites in carbon materials. A low ratio of amorphous carbon with a high degree of disordering corresponds to a high concentration of surface active sites associated with the edges of graphite-like layers. The catalytic performance combined with characterization results demonstrates that the edges of graphite carbon are active sites in HI decomposition. A computational chemistry study is also conducted to illustrate the dominant role of edge sites in the reaction. The calculation results build a detailed mechanism of the catalytic decomposition of HI over the carbon materials and verify that the adsorbed I on the edge sites facilitate the HI decomposition.

© 2014 Elsevier B.V. All rights reserved.

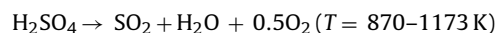
## 1. Introduction

Hydrogen is considered an alternative source of energy because of its environmentally friendly characteristics. An efficient hydrogen production system is necessary in developing a hydrogen energy system. The thermochemical water-splitting cycle, which produces hydrogen and oxygen from water through a series of correlative chemical reactions, has attracted much attention in current research. The inputs in thermochemical cycles are heat and water; other intermediates are not consumed and are recycled in the process. Among various potential thermochemical cycles, the sulfur–iodine (SI) thermochemical cycle presents significant advantages. The SI cycle involves three reactions:

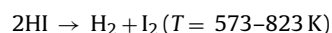
Bunsen reaction :



Sulfuric acid decomposition :



Hydrogen iodide decomposition :



The decomposition of hydrogen iodide (HI) serves as the step toward hydrogen evolution in several thermochemical water-splitting steps. However, the homogeneous gas-phase conversion during the decomposition is rather low, occurring below 833 K. The use of catalysts is therefore desirable to accelerate the reaction rate. Early studies that sought to identify active catalysts were mainly conducted in the late 1970s and 1980s and have been well summarized by O'Keefe et al. [1]. A series of activated carbon (AC)-based catalysts have also been discussed recently [2–8]. Such studies lead to the conclusion that the Pt catalysts have the best catalytic performance, but their catalytic activities are only slightly higher than those of unmodified ACs above 700 K. Thus, AC is an economical alternative to noble metal catalysts for large-scale hydrogen production.

AC has been studied in many catalytic reactions for its high surface area, well-developed porous structure, and variable

\* Corresponding author. Tel.: +86 571 87952040; fax: +86 571 87951616.  
E-mail address: [zhangyw@zju.edu.cn](mailto:zhangyw@zju.edu.cn) (Y. Zhang).

surface compositions. The performance of a catalyst depends on the availability of suitable active sites capable of chemisorbing the reactants and forming surface intermediates of adequate strength. In last few decades, many papers focused on the structural characterization and nanostructures of AC have been published [9–14], given that knowledge of such structures are bound to directly affect the number of reactive sites [15–17]. The structural analysis of ACs and other disordered carbons provides a direct perspective for the quantitative analysis of reactive sites [15,18]. The structure of the nano-crystalline forms of AC generally consists of what can be described as disordered graphite-like layers with very weak inter-layer correlations or random stacking [19,20]. The disordered graphite-like layers are mainly composed of micro-graphite in nanometer scale with a short-range order that varies across different carbon materials. The inter-layer correlations are usually made up of aliphatic carbon or other saturated carbon species. Various characterization techniques, such as transmission electron microscopy (TEM), scanning electron microscopy (SEM), atomic force microscopy (AFM), scanning transmission electron microscopy (STEM), X-ray diffraction (XRD), and Raman spectroscopy, have been utilized in examining the structure of carbon materials. Raman spectroscopy has become the standard characterization method for carbon materials because of its capacity to provide information on the crystalline size, ratio of  $sp^2$  (graphite-like layers) to  $sp^3$  (inter-layer correlations), ordering of the graphite-like layers, and many other such unique data [10,21–23]. XRD is the most common method used in describing carbon materials in terms of various parameters, including average in-plane length ( $L_a$ ), average height ( $L_c$ ), average inter-planar distance ( $d_{002}$ ), 3D ordering of the graphite-like layers, and density and type of defects [14,24]. Other characterization methods, such as AFM and STEM, provide an accurate representation of the carbon structure and defect content.

In this study, the characteristics of AC and other three carbon materials were examined through a series of instruments and were associated with the catalytic activities of the carbon materials. A traditionally structured model was applied to the four materials for the quantitative analysis of the carbon structure. The quantities of the active sites in the materials were evaluated through an effective structural model with several characterization methods. A detailed mechanism of the catalytic decomposition of HI over the carbon materials was also established.

## 2. Experimental setup

### 2.1. Catalyst preparation

The four samples—AC, multiple-walled carbon nanotubes (MWCNT), carbon black (CB), and carbon molecular sieves (CMS)—were obtained from JCNANO Co. The AC used in this study is coconut-shell activated carbon, and it is produced by  $ZnCl_2$  activation. They were crushed into powder (40–60 ASTM mesh fraction) and vacuum dried for 2 h. All of the four samples were heated from room temperature to 873 K under flowing nitrogen at 5 K/min and then kept at that temperature for 3 h to remove their functional groups.

### 2.2. Catalyst characterization

The porosity of each sample was analyzed using a Micro-metrics 2020 ASAP porosimeter. Their nitrogen adsorption and desorption isotherms were obtained at 77 K after degassing. The BET surface area was calculated from the  $N_2$  adsorption data at relative pressures of  $0.05 < P/P_0 < 0.3$ . The total pore volume was calculated from the amount of  $N_2$  adsorbed when  $P/P_0 = 0.99$ . The

density functional theory (DFT) model was used to analyze the results.

The XRD patterns of the catalysts were acquired using a Rigaku K/MAX2550/PC XRD. Cu K- $\alpha$  radiation was employed at a working voltage and current of 40 kV and 100 mA, respectively. The XRD patterns were recorded at intervals of  $0.02^\circ$  in the range of  $10^\circ \leq 2\theta \leq 80^\circ$ . The PeakFit v4.12 was used to deconvolute the diffraction patterns in the  $2\theta$  region of  $15\text{--}32^\circ$ . The broad hump in this region was fitted to two Gaussian peaks around  $20^\circ$  and  $26^\circ$ , which represented the  $\gamma$ - and  $\pi$ -bands ( $d_{002}$ ), respectively. The areas below the  $\gamma$ - and  $\pi$ -peaks are theoretically acknowledged to be equal to the number of aromatic and aliphatic carbon atoms, respectively. The aromaticity ( $A_{\text{arom}}$ ) of the studied carbon materials—the ratio of carbon atoms in aromatic rings to the aliphatic chains—was calculated based on the literature [25].

Scanning electron microscopy (SEM) observation of the catalysts was performed on a Hitachi S-4800 operated at 5–20 kV. Samples were mounted on aluminum stubs using double-sided tapes. The images were obtained in the secondary electron mode in conjunction with SEM imaging.

The crystallite structure of the four catalysts was characterized by high-resolution transmission electron microscopy (HRTEM) (Philips Tecnai G2 F20). The powders were gently ground and dispersed in carbon film-coated copper grids by dipping the grids into a methanol suspension of the powder.

The surface oxygen-containing groups of the supports were characterized by the temperature-programmed desorption mass spectrometry (TPD-MS) method with an apparatus consisting of a Micromeritics AutoChem II 2920 and a Hiden QIC20 quadrupole mass spectrometer. Approximately 0.1 g of the sample was loaded into a quartz U-tube with an inner diameter of 10.0 mm. Prior to the desorption experiments, the samples were degassed for 1 h in a helium stream [ $50\text{ cm}^3$  (STP)/min] at 383 K. The temperature was then increased to 1373 K at a heating rate of 10 K/min. The evolution of carbon dioxide ( $m/z = 44$ ) and carbon monoxide ( $m/z = 28$ ) was monitored by the quadrupole mass spectrometer.

X-ray photoelectron spectroscopy (XPS) measurements were conducted on a Thermo XPS ESCALAB 250Xi instrument with Al K $\alpha$  (1486.8 eV). The X-ray source and samples were maintained under ultra-high vacuum conditions ( $<10^{-9}$  mbar). The binding energies were calibrated using the containment carbon (C 1s = 284.5 eV). XPS Peak 4.1 was applied to deconvolve the C 1s peaks using the Shirley-type baseline and an iterative least-squared optimization algorithm.

A model of the DXR smart Raman spectrometer (Thermo Fisher, USA) was used to analyze the structure of the materials at a laser wavelength of 532 nm, power of 3.0 mW, and collection exposure time of 7.5 s. The deconvolution of the Raman spectra was conducted using PeakFit v4.12.

### 2.3. Activity tests

Fig. 1 shows the schematic illustration of the experimental setup consisting of quartz and glass. The catalytic reaction was conducted at the atmospheric pressure in a quartz tube reactor (inner diameter = 18 mm) placed vertically in an electrically heated tube furnace. The heated evaporator was set at 433 K to ensure the flash vaporization of the HI solution flash.  $N_2$  was used to drive the vaporized HI through the system. Unreacted HI,  $H_2O$ , and  $I_2$  were trapped and collected through a spiral condenser. The gaseous products ( $H_2$  and  $N_2$ ) were analyzed using an online hydrogen analyzer (K522, HITECH INSTRUMENTS Ltd) after purification with NaOH solution and silica gel. Other apparatuses included a BT100-2J peristaltic pump (LongerPump) and a mass flow controller (Alicat Scientific) for  $N_2$ . The catalytic decomposition of HI was performed from 573 K

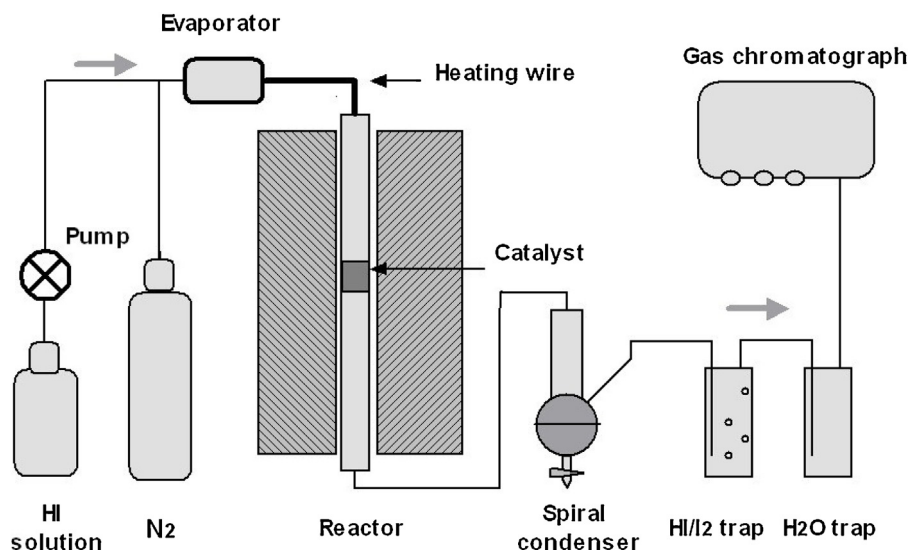


Fig. 1. Schematic of experimental catalyst activity test system.

to 823 K. Approximately 1 g of the catalysts was uniformly mixed with coarse chips of quartz fixed in the quartz tube reactor. The HI solution (55.5 wt.%) was pumped into the evaporator at the operating temperature and a flow rate of 0.7 mL/min, and the flow rate of  $N_2$  was maintained at 60 mL/min. The measurements were conducted under a steady hydrogen production condition (the initial conditions of the experiments were unstable).

### 3. Results and discussion

#### 3.1. Catalyst analysis

##### 3.1.1. Nitrogen physisorption

Fig. 2 shows the nitrogen physisorption isotherms displayed by the samples analyzed in this study. The shape of the isotherms of AC and CMS, which shows a sharp increase in adsorption at very low relative pressures and a plateau-like adsorption at high relative pressures, indicates an almost entirely microporous material. Sample CB and MWCNT yield the type-IV isotherm (following the BDDT classification), which is a characteristic of mesoporous materials.

The textural properties of all of the materials are presented in Table 1. CMS sample shows the highest surface area of  $787.6 \text{ m}^2/\text{g}$ , the CB has the least surface area of  $106.4 \text{ m}^2/\text{g}$ . The BET surface areas and pore volumes are related to the pore structure. Among

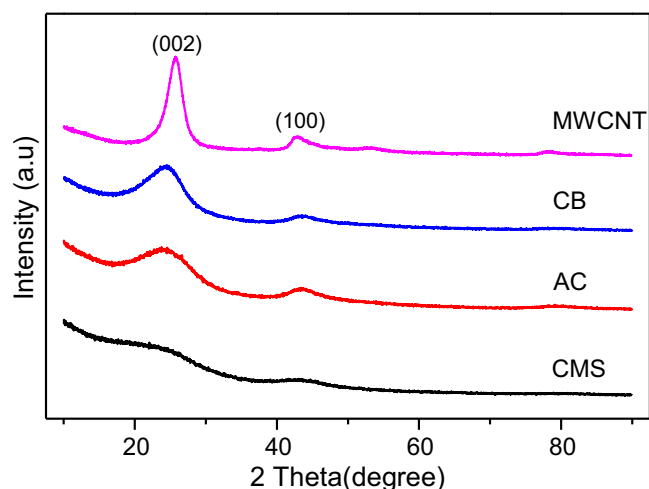


Fig. 3. XRD patterns of the CMS, AC, CB and MWCNT samples.

the samples, CMS and AC have the largest surface area, which can be attributed to their microporous structure. CB and MWCNT, which have a mesoporous structure, possess less surface areas and larger pore volumes than CMS and AC.

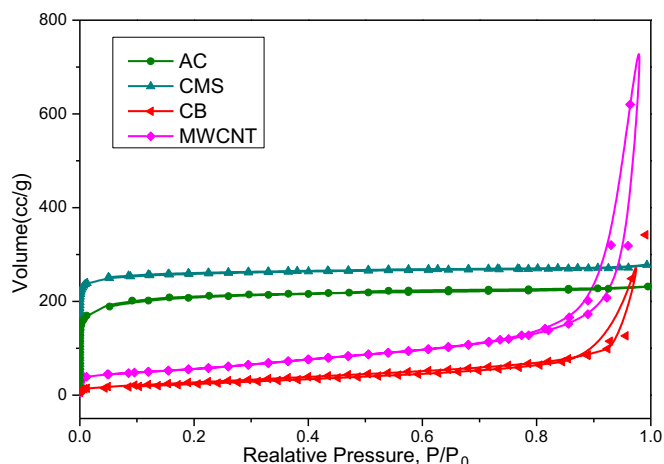


Fig. 2. Nitrogen-physisorption isotherms at 77 K of the four materials.

##### 3.1.2. XRD

XRD is the most commonly used technique in the quantitative analysis of molecular-scale structures. Fig. 3 displays the XRD of the four carbon materials. Two diffraction peaks at around  $2\theta = 26^\circ$  and  $45^\circ$  are observed in all of the four samples, corresponding to (002) and (100) diffractions of carbon, respectively. The presence of a clear (002) diffraction peak indicates the existence of a graphite-like structure (graphite carbon). The trend of the (002) diffraction peaks exhibits a gradual weakening and broadening in the order of MWCNT, CB, AC, and CMS, implying a decreasing graphitizing degree. The latter three samples particularly exhibit high background intensity, indicating that these materials contain a proportion of highly disordered materials in the form of amorphous carbon. These findings show that the crystallites in all of the carbon materials have intermediate structures between graphite and amorphous states, as shown in Fig. 4. The carbon materials consist mainly of two parts: graphite carbon with randomly stacked layers and amorphous carbon along the layer linkages or

**Table 1**

Textual properties and TPD-MS results of the four carbon materials.

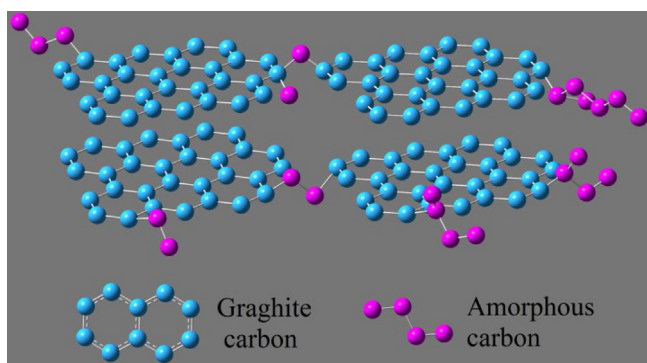
Sample	BET (m <sup>2</sup> /g)	ESA <sup>a</sup> (m <sup>2</sup> /g)	TPV <sup>b</sup> (cm <sup>3</sup> /g)	CO <sub>2</sub> <sup>c</sup> (μmol/g)	CO <sup>c</sup> (μmol/g)	CO <sub>2</sub> + CO
CMS	787.6	72.6	0.43	293.15	770.71	1063.86
AC	649.7	95.8	0.36	193.33	724.50	917.83
CB	106.4	141.3	0.53	126.33	707.17	833.50
MWCNT	200.4	218.5	1.29	133.16	198.65	331.81

BET surface area, BET; external surface area, ESA; total pore volume, TPV.

<sup>a</sup> From *t*-plot method.<sup>b</sup> Calculated at *P*/*P*<sub>0</sub> = 0.99.<sup>c</sup> Amounts of the CO and CO<sub>2</sub> obtained by integration of the areas under TPD peaks.**Table 2**

Structure parameters extracted from the curve-fitting of XRD spectra.

Sample	<i>d</i> <sub>002</sub> (nm)	<i>L</i> <sub>c</sub> (nm)	<i>m</i>	<i>L</i> <sub>a</sub> (nm)	<i>A</i> <sub>arom</sub> (%)	<i>A</i> <sub>amo</sub> (%)	<i>N</i> = <i>A</i> <sub>arom</sub> / <i>m</i>
CMS	0.3716	1.276	3.4	3.917	75.4	24.6	0.221
AC	0.3709	1.286	3.5	4.228	85.7	14.3	0.245
CB	0.3644	1.597	4.4	4.295	89.3	10.7	0.202
MWCNT	0.3458	3.109	9.0	7.459	90.8	9.2	0.101

**Fig. 4.** A traditional structure model used for quantitative analysis of the four carbon materials.

edges. The structure of the graphite carbon can be described by a combination of several parameters, as those listed in Table 2. The calculation of these parameters is based on the Bragg and Scherrer equations, according to the literature [25,26]. The relative size of the graphite carbon can be determined through the following equation:

$$m = \frac{L_c}{d_{002}}$$

Table 2 shows that CMS has the smallest size of graphite carbon among the four materials. The size of the crystallite generally has a negative correlation with the density of the edge sites, but this theory is untenable for disordered carbon materials. The diffraction profiles show the presence of a clear asymmetric (002) band around 26°, suggesting the existence of another band (γ) on its left hand side. A representative fit of two Gaussian peaks for the bands around 20° and 26° is conducted for the quantitative analysis of the carbon structure, in accordance with the literature [25]. The *A*<sub>arom</sub> represents the concentration of graphite carbon in the carbon materials; thus, the quantity of the edge sites can be determined based on the size of graphite carbon and *A*<sub>arom</sub>. According to the structure model (as shown in Fig. 4), it could be noted that the amount of the edge sites is directly proportional to the *A*<sub>arom</sub>, while inversely proportional to the size of graphite carbon. Therefore, we deduce that the *A*<sub>arom</sub>/*m* can be used to compare the amount of edge sites. Although CMS has the smallest graphitic carbon among all of the materials, AC possesses the highest concentration of edge sites owing to its high concentration of graphite carbon.

### 3.1.3. HRTEM

HRTEM was used to characterize the microstructure of the four carbon materials. The HRTEM images shown in Fig. 5 indicate that the structure of short-range graphite carbon is present in the four carbon materials. An apparent decrease also occurs in the structure ordering of the graphite carbon, which is consistent with the results of our XRD measurements. The parameters *L*<sub>a</sub>, *L*<sub>c</sub>, and *m*, which are used to depict the short-range graphite carbon, can be directly observed in the HRTEM images. All of these parameters match the value calculated in Table 2. The size of the graphitic carbon has a negative correlation with the degree of disordering of the carbon structure. Among all of the samples, CMS possesses the most disordered structure with the smallest size of short-range graphitic crystallites. In contrast to that in AC and CMS, the graphitic carbon in CB has a lower disordering and therefore a larger size of graphitic crystallites.

### 3.1.4. Raman spectroscopy

Raman spectroscopy is traditionally used to study the structure of carbon materials. The Raman spectra of the carbon materials generally present two first-order bands in the 1000–3000 cm<sup>−1</sup> region: a D band at approximately 1350 cm<sup>−1</sup> and a G band at approximately 1580 cm<sup>−1</sup>. In carbon materials with a poor structural ordering, additional bands appear in the first-order region around 1200, 1350, 1500, and 1620 cm<sup>−1</sup>, where the 1200 cm<sup>−1</sup> (D4) band appears only in very poorly organized carbon materials [27]. The 1580 cm<sup>−1</sup> band (G band) corresponds to the in-plane Raman vibration mode of graphite and is characteristic of the ideal graphitic lattice vibration mode [28,29]. The 1350 cm<sup>−1</sup> band (D band), commonly called the defect band, is attributed to in-plane defects and heteroatoms [20,27,30]. The G and D bands are usually compared to evaluate the graphitization degree of carbon materials. In this region, the intensity excess in the valley between the D and G bands indicates the existence of another band around 1500 cm<sup>−1</sup> (D3), which appears as a fairly broad band in poorly crystallized carbon materials only. This band has been attributed to the defects outside the planes of aromatic layers, such as tetrahedral carbon.

Fig. 6 shows the Raman spectra of the four carbon materials in the region from 1000 to 2000 cm<sup>−1</sup>. All of the curves exhibit two relatively broad Raman bands at about 1340 and 1590 cm<sup>−1</sup>, corresponding to the D and G bands, respectively. For further analysis, the Raman spectra were deconvoluted with a multiple peak fit with combinations of Gaussian and Lorentzian functions [27,30,31]. The deconvolution results are presented in Fig. 7 and Table 3. Based on the original correlation of Tuinstra and Koenig [32], the D/G band



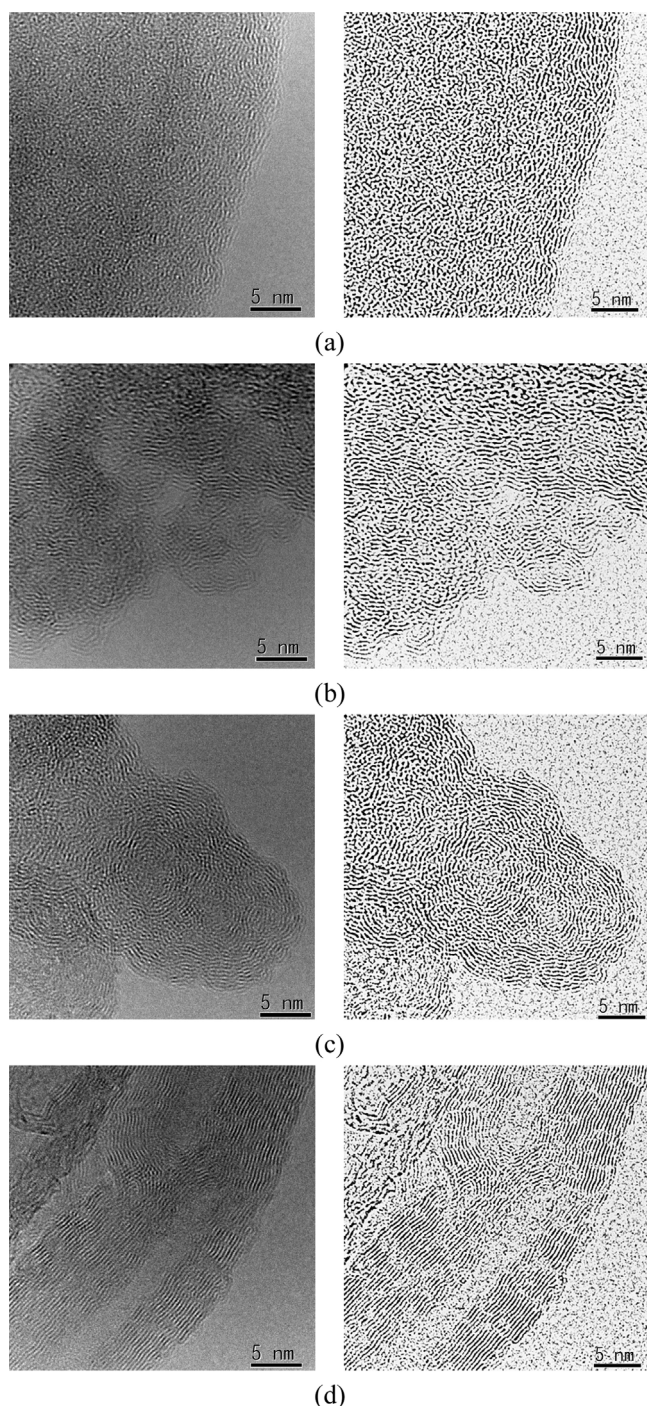


**Fig. 5.** The HRTEM images of the four carbon materials, (a) CMS; (b) AC; (c) CB; and (d) MWCNT.

intensity (peak area) ratio, i.e.,  $I_D/I_G$ , is inversely correlated with the crystallite lateral diameter  $L_a$  determined from XRD. The crystallite lateral diameter  $L_a$  of the used excitation length at 532 nm was evaluated using the following relation:

$$L_a = 4.96I_G/I_D \text{ (nm)}$$

The  $L_a$  values obtained from the Raman measurements are lower than those from XRD. This finding may be attributed to the characterization methods, in which Raman spectroscopy is more sensitive to small than large crystallites, whereas XRD is more sensitive to large than small crystallites [31,33].

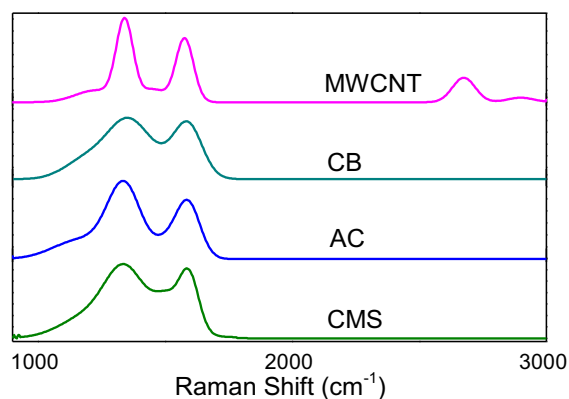


**Fig. 6.** Raman spectra of the four carbon materials.

The D/G band intensity ratio is used to compare the structural ordering of the carbon materials, together with the full width at half maximum (FWHM) and position of the main bands. There is no significant shift in the D and G bands of any of the four carbon materials. However, the FWHM of the D band and the ratio  $I_D/I_G$  suggest the following sequence in terms of structure ordering: CMS < AC < CB < MWCNT, which is consistent with the results in XRD and HRTEM characterizations. From a traditional perspective, a lower ordering with smaller  $L_a$  implies more edge sites. However, in the case of carbon materials with a large number of tetrahedral carbons corresponding to D3 and D4 bands, the quantity of the edge sites is not merely proportional to the disordering of the carbon structure. In fact, the quantity of edge sites not only depends on the disordering and size of the graphite-like structure but is also related to the ratio of graphite-like and amorphous carbon in carbon materials. The D band relates to in-plane defects and heteroatoms and  $I_D$  stands for the edge sites in graphitic carbon,  $I_{Tot}$  takes all the different carbon structures into account, including in-plane carbon atoms and the edge sites of graphitic carbon, the aliphatic carbon. Therefore, the new ratio  $I_D/I_{Tot}$  ( $I_{Tot} = I_D + I_G + I_{D3} + I_{D4}$ ) provides a more accurate comparison for the number of edge sites in disordered carbon materials instead of  $I_D/I_G$ . The obtained  $I_D/I_{Tot}$  values indicate that AC possesses the largest number of edge sites among the four carbon materials, which is consistent with the XRD results.

### 3.1.5. XPS

Both XPS and TPD-MS analysis are used to study the surface properties of carbon materials. Given that XPS characterization provides a better understanding of surface structures than other techniques, the TPD-MS results listed in Table 1 can serve as complementary data. For a deeper insight into the XPS results, the C 1s spectra was deconvoluted by considering five different contributions, following the literature [34]. The deconvolution results are presented in Fig. 8 and Table 4. The relative intensity of the defect peak corresponds to the aliphatic carbon present in defects and inter-layer correlations, and it also indicates the degree of the disordering and amorphousness of the carbon materials [35]. The CMS representing the highest degree of disordering and amorphousness is also reflected in the surface properties. The aliphatic carbon contents of the four carbon materials are in good agreement with the XRD results. The XPS results also contain information on the surface functional groups located at the edge of the graphite-like layers. Some studies have also reported that the TPD techniques can be used to quantify the active sites [18]; therefore, the relative contents of the surface functional groups can also offer general information on the number of edge sites for carbon materials. The quantitative determination of functional groups was based on CO and CO<sub>2</sub>, as the oxygen containing chemical groups are

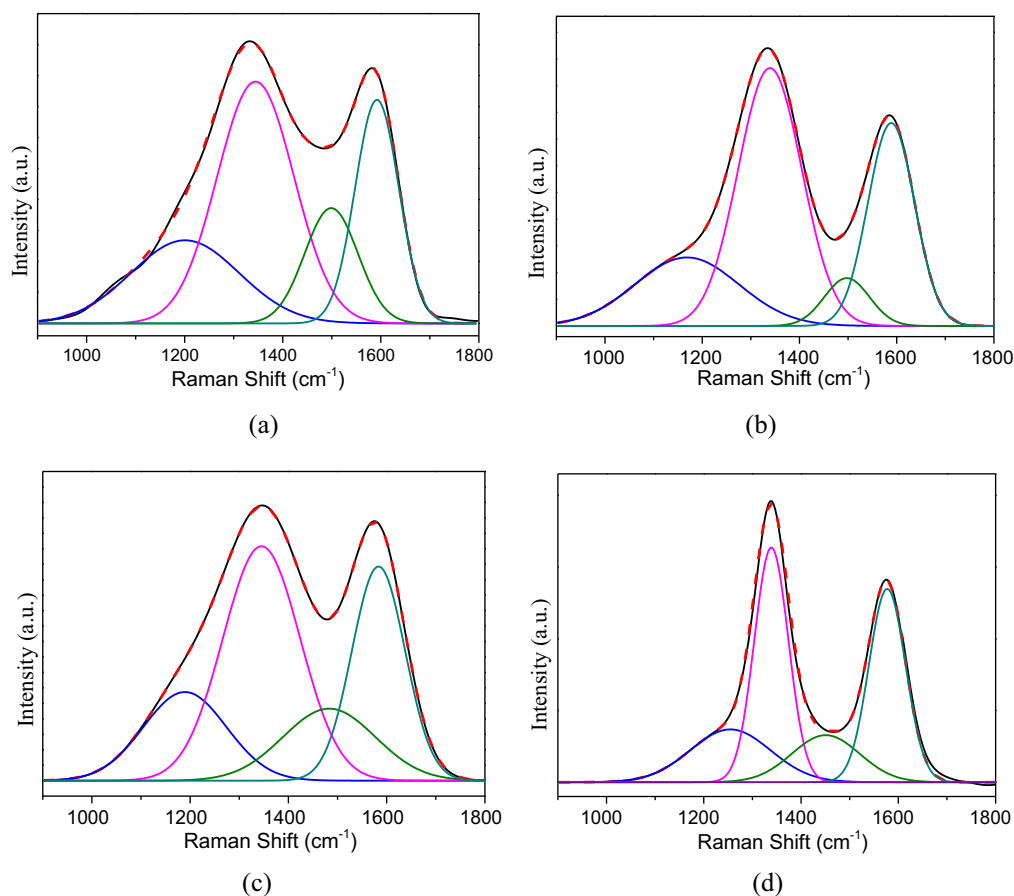


Fig. 7. Deconvolution of the first order Raman spectra of the four carbon materials: (a) CMS; (b) AC; (c) CB; and (d) MWCNT.

Table 3

Raman parameters of the four carbon materials.

Sample	Position (cm <sup>-1</sup> )	Intensity	FWHM (cm <sup>-1</sup> )	I/I <sub>Tot</sub>	I <sub>D</sub> /I <sub>G</sub>	L <sub>a</sub> (nm)
CMS						
D	1344.6	7675.3	184.8	42.7%	2.21	2.23
D3	1499	2533.2	127.9	14.1%		
G	1592.1	4035.8	105.0	22.4%		
D4	1200.8	3711.2	260.0	20.7%		
AC						
D	1339.3	7945.9	154.5	46.7%	1.74	2.85
D3	1497.6	1040.8	109.2	6.1%		
G	1588.7	4575.5	113	26.9%		
D4	1168.6	3438.1	251.9	20.2%		
CB						
D	1345.3	2994.3	185.5	41.6%	1.59	3.12
D3	1483.0	1098.5	221.6	15.3%		
G	1583.5	1883.4	127.7	26.2%		
D4	1189.3	1213.9	199.0	16.9%		
MWCNT						
D	1339.0	2874.7	82.5	35.6%	1.13	4.39
D3	1450.7	1143.6	163.4	14.1%		
G	1577.2	2545.2	88.7	31.4%		
D4	1254.6	1519.0	193.9	12.1%		
2D	2674.4	1428.7	119.1			
2D'	2897.7	296.2	128.6			

Table 4

Position and distribution of the C 1s spectral region peaks from XPS of the four materials.

Peak position (eV)	Assessment	Peak contribution (%)			
		AC	CMS	CB	MWCNT
284.4	C (aromatic)	58.5%	56.0%	68.3%	71.8%
285.2	C (aliphatic "defects")	15.6%	24.6%	10.5%	8.0%
286.0	C—OH; C—O—C	9.5%	6.8%	11.1%	8.7%
289.4	COOH	12.1%	12.7%	10.1%	4.0%
291.0	$\pi \rightarrow \pi^*$	4.3%	—	—	7.5%

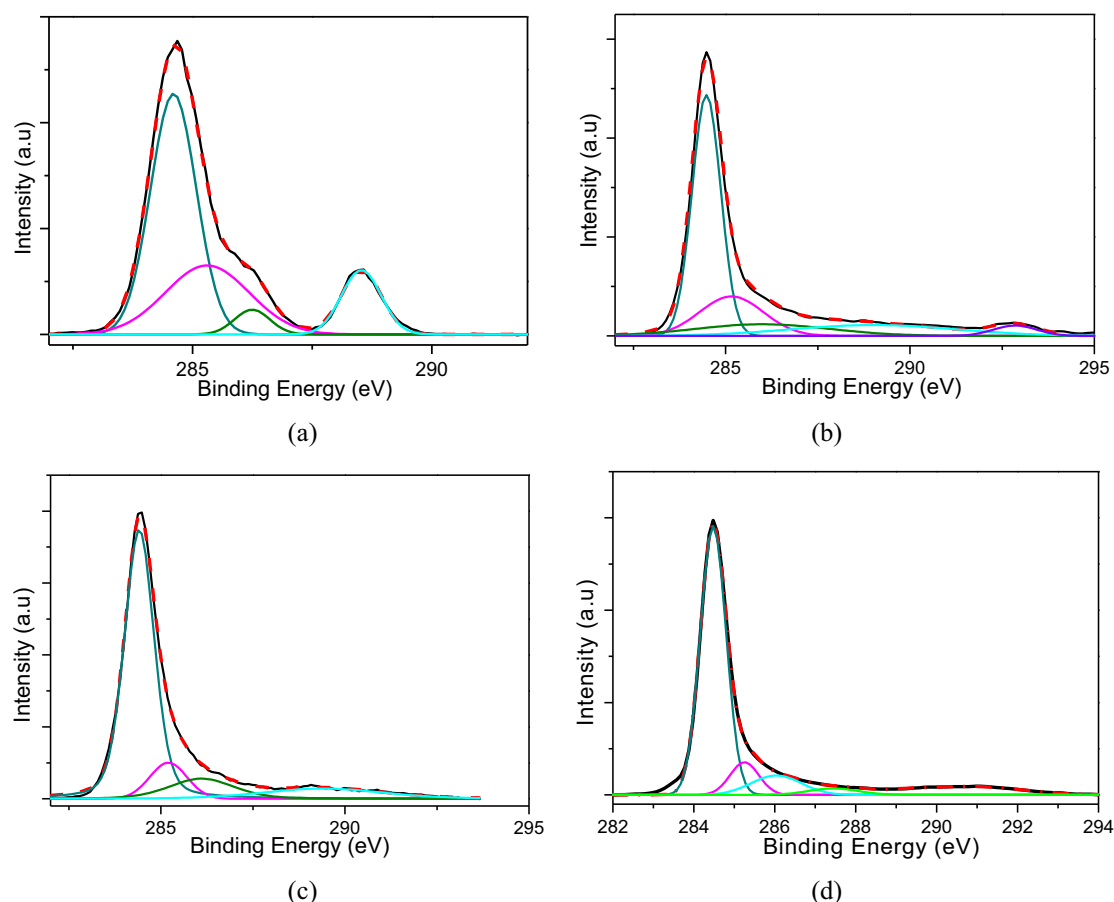


Fig. 8. Deconvolution of the XPS C 1s spectra: (a) CMS; (b) AC; (c) CB; and (d) MWCNT.

decomposed mainly to CO and CO<sub>2</sub>. Before the TPD-MS experiment, the mass spectrometer was calibrated using CO ( $m/z=28$ ) and CO<sub>2</sub> ( $m/z=44$ ) gases. During the experiment, the gas phase was continuously analyzed quantitatively by the mass spectrometer, and the gas releasing curves were displayed in the supplementary data (Figs. 1 and 2). The total amount of CO and CO<sub>2</sub> listed in Table 1 was computed by time integration of the TPD-MS curves. Both XPS and TPD-MS results illustrate that, among all of the samples, AC has the largest number of edge sites, which verifies our Raman and XRD results.

Although CMS has the most disorganized structure among all of the samples, its high concentration of amorphous carbon decreases its edge sites. Thus, structure ordering should not be the only parameter to determine the quantity of edge sites; the amorphous character of the material must also be considered, particularly that of highly disordered carbon materials.

### 3.2. Catalytic performance and discussion

Fig. 9 shows the results of HI conversion at 573–773 K for various catalysts. The results of the thermodynamic and blank tests are also plotted in Fig. 9. The results of thermodynamic test A were obtained from the literature [1], whereas those of thermodynamic test B were obtained using FactSage (a commercial software based on complex thermochemical databases). Generally, there are three types of carbon atoms existing in the four carbon materials: carbon atoms in-plane in graphitic carbon, edge carbon atoms in graphitic carbon, and aliphatic carbon atoms in inter-layer correlations. Aliphatic carbon atoms are usually saturated and

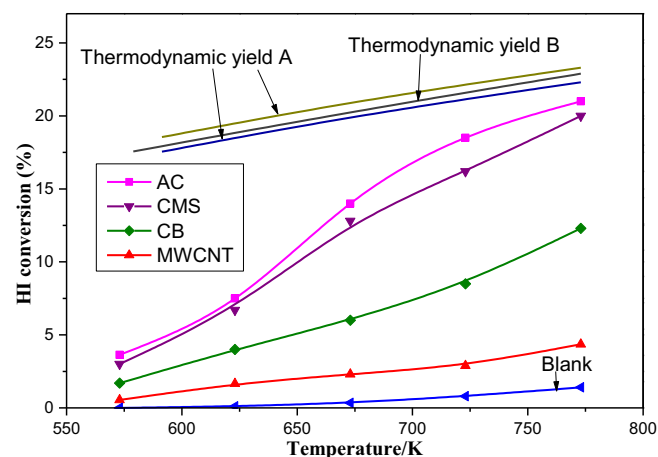


Fig. 9. HI conversions with temperature for different carbon structure catalysts.

present quite stable state, and they would have little effect on the catalytic decomposition. On the contrary, carbon atoms in graphitic carbon usually play positive roles in catalytic reactions as they are unsaturated and active. Above all, the edge sites behave more active and unstable than the in-plane atoms, thus they would act as adsorption sites and contribute to the reactions. The catalytic performance of the four materials is proportional to the quantity of active sites; AC shows the highest catalytic activity, followed by CMS, CB, and then MWCNT. The catalytic performance verifies that carbon atoms located at the graphite carbon edges are active sites in



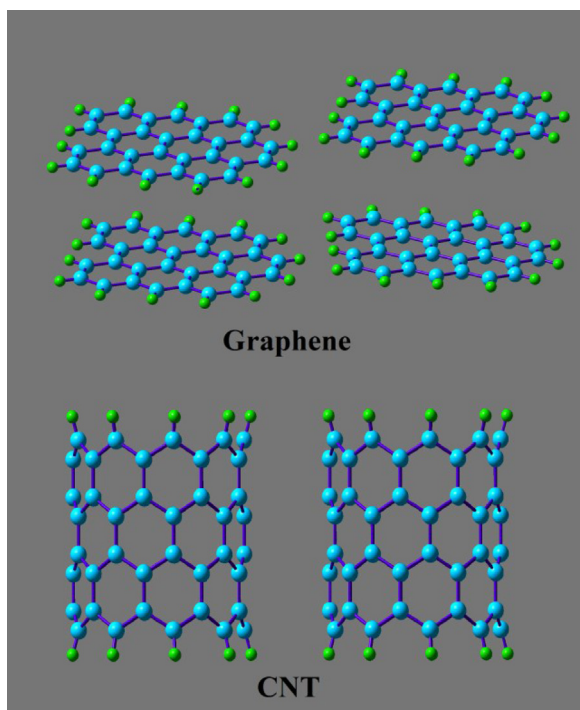


Fig. 10. The carbon structure of future potential catalysts for HI decomposition.

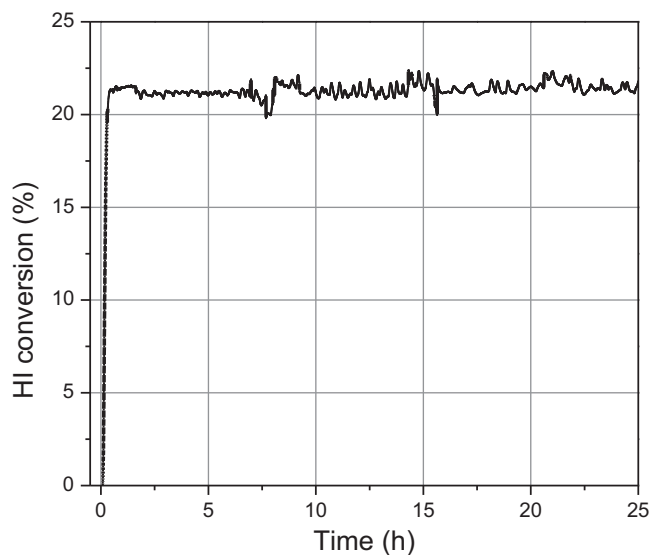


Fig. 11. Catalyst stability test result of the AC sample at 500 °C.

HI decomposition. At high temperatures, the conversion of HI over AC is near the thermodynamic equilibrium rate, indicating the vast potential of carbon materials to be used as catalyst for HI decomposition. Although functional groups have some influence on catalytic performance, the number of edge sites is believed to be the dominant factor. Moreover, the functional groups have been removed to the largest possible degree, and thus the effects of the functional groups are ignored in this study.

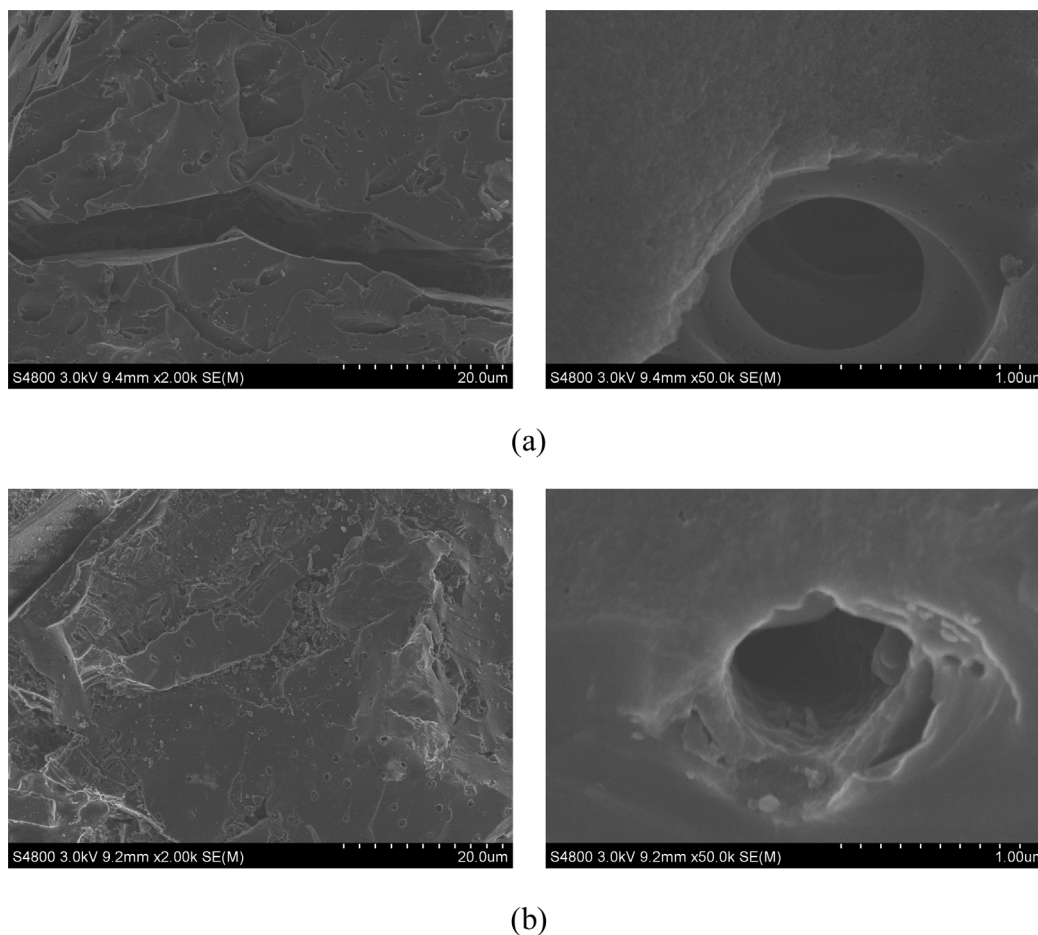


Fig. 12. The SEM images of the AC sample: (a) before reaction and (b) after reaction.



The results above indicate that the effective way to enhance the HI conversion is to increase the amount of edge sites as much as possible. Combined with several characterization results, a standard is put forward to measure the amount of edge sites for carbon materials that carbon structures with short crystallite lateral diameter and less amorphous carbon contents present the largest amount of edge sites. AC materials present excellent catalytic performance in the HI decomposition should be benefit from its activation methods which result into the small size of graphitic carbon and low contents of amorphous carbon. The conclusions we draw from this research also point out a direction for the activation methods to improve the catalysts activity of AC materials. With new carbon materials being explored, we deeply believe that the graphene and single-wall carbon nanotube with short  $L_a$  can serve as potential carbon catalysts, as shown in Fig. 10.

A long run test is conducted to check the stability of the AC sample as it presents the highest catalytic performance. The operation temperature is 500 °C, and the test time is 24 h. As shown in Fig. 11, the measured HI conversion values recorded every 10-s are nearly 22% (close to the thermodynamic yield at 500 °C) and remain constant along the experiment time. Several sharp drops, originated from the refilling of HI, appear at yield. The stability test proves that this catalyst is stable and active at current condition.

The characterization of the used catalyst has also been carried out to study the change of the catalyst during the decomposition. The SEM images of AC sample before and after reaction were displayed in Fig. 12. No remarkable change could be noted in the surface of AC, but the surface in the pore became rough and corroded comparing to the fresh sample. The corrosion in the pore could be attributed to the HI and H<sub>2</sub>O at high temperatures. The pores in the catalysts containing large amount of active sites play important roles in HI decomposition, thus the corrosion should be noted. The HI conversion values remain constant during our stability test, and we conclude that the change in the pore would not affect HI decomposition in several hours, while long-term test remains to be studied.

### 3.3. Mechanism discussion

The experimental results prove that edge sites of graphite carbon are the active sites in HI decomposition, and we have also conducted DFT calculation to verify this. Although the edge sites are always occupied with heteroatoms forming surface functional groups, only the unsaturated atoms located at the edge sites are discussed in this study for the initial analysis of the mechanism of HI decomposition over carbon materials.

The mechanism was established based on the DFT calculation using Gaussian 03 [36], with the B3LYP functional and the 3-21G\*\* basis set. Following the literature [37,38], a zig-zag structure with three vacant edge sites was adopted for the carbon catalyst model. The well-established pathway for the catalytic decomposition of HI over carbon materials is composed of several transition states, intermediates, and products (Fig. 13). The intrinsic reaction coordinate was used to verify all of the transition states during the decomposition process. The initial HI molecules were chemisorbed on the unsaturated edge site; the findings show that HI tends to adhere to the zig-zag surface with the I ending toward the surface. After structural optimization, the H atom is separated from the I atom and attached to the vacant site, resulting in the cleavage of H–I bond to form a stable intermediate M1, via a transition state TS1. The edge sites of the graphite carbon, which provide active sites for the adsorption and interaction of HI molecules, have a dominant role in the first section. The intermediate M2 has an active role in the next step, during which the adsorbed I on the graphite carbon tends to be conducive to the adsorption of unreacted HI molecules.

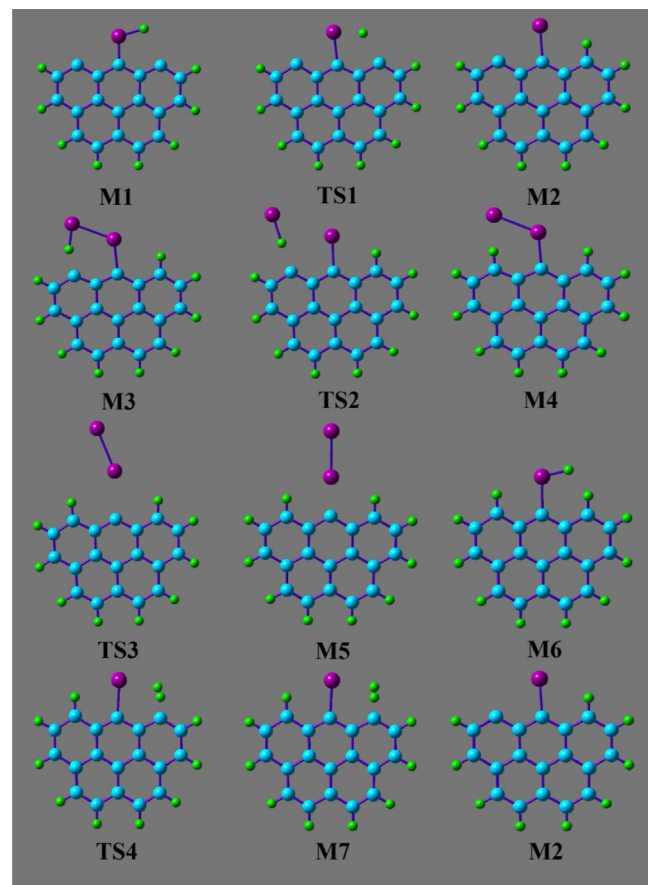


Fig. 13. The well-established pathway for the catalytic decomposition of HI over carbon materials.

After adsorption, the adsorbed HI reacts with the vacant edge sites, resulting in the cleavage of the H–I bond and formation of a stable intermediate M4. The interaction between the adsorbed I on the graphite carbon and the edge site then weakens, causing the dissociation of I<sub>2</sub> via a transition state TS3. In this section, the adsorbed I on the graphitic carbon has a positive role in the formation of I<sub>2</sub>, such that it can drive the adsorption of unreacted HI and facilitate the dissociation of I<sub>2</sub> [6]. The last section involves the yield of H<sub>2</sub>, which is the process with the highest energy barrier during the reaction. The desorption of I<sub>2</sub> involves the concomitant generation of a vacant edge site between two adsorbed H. Unreacted HI molecules follow the previous adsorption step to form a stable intermediate M6. The next step involves concomitant bond formation and bond cleavage, in which the H–I bond is broken and the H–H bond is formed via TS4 to produce H<sub>2</sub> and a stable intermediate M2. Given that the energy barrier to the following step M6 → TS4 is relatively high, the formation of H<sub>2</sub> is considered to be the rate-determining step in the path.

The DFT calculation verifies the significant function of edge sites in the reaction, which serve as adsorption sites initially and then take part in the breakage and formation of the bonds. The reaction pathway shows that the adsorbed I on the edge sites have a dominant role in the decomposition. Besides, the reactions between the adsorbed I and HI molecules are demonstrated to be dominant during the HI catalytic decomposition process, which is consistent with the results reported in the literature [6,39,40]. The dissociation of the H<sub>2</sub> has the highest energy barrier, leading to the introduction of some transition metals to support the carbon materials and facilitating the formation of H<sub>2</sub> [41,42].

#### 4. Conclusions

In this study, four carbon materials were examined through a series of characterization methods and an HI decomposition test. A traditional structure employed on the carbon materials contributed to the quantitative analysis of the four samples. The catalytic performance combined with characterization results verifies that the edges located at the graphite carbon are the active sites in HI decomposition. The DFT calculation results confirm important roles of the edge sites in the reaction.

The nitrogen physisorption results illustrate that AC and CMS have a microporous structure, whereas CB and MWCNT have a mesoporous structure. This difference is related to the size and ordering of the graphitic carbon in the carbon materials. The HRTEM images show that the microstructures of the four materials contain short-range graphite carbon with varying disordering and sizes. The XRD and Raman spectroscopy results indicate that lesser stacked graphite-like layers and shorter lateral diameter  $L_a$  result in higher disordering structure. The degree of disordering is not the only factor determining the quantity of active sites. The aliphatic carbon existing in the inter-layer correlations decreases the amount of graphite carbon and occupies the edge sites, thus inhibiting the formation of active sites in carbon materials. The lower ratio of amorphous carbon and the higher degree of disordering suggest a higher concentration of surface active sites associated with the edge sites at graphite-like layers, which contribute to the highest catalytic performance. The mechanism of the HI catalytic decomposition over carbon materials is also described. The calculation results show that the adsorbed I on the edge sites facilitates the decomposition. Meanwhile, the formation of  $H_2$  is the rate-determining step in the path.

#### Acknowledgements

This work has been financially supported by National Natural Science Foundation of China (51276170). The authors gratefully acknowledge the support.

#### Appendix A. Supplementary data

Supplementary data associated with this article can be found, in the online version, at <http://dx.doi.org/10.1016/j.apcatb.2014.11.026>.

#### References

- [1] D. O'Keefe, J. Norman, D. Williamson, *Catal. Rev.-Sci. Eng.* 22 (1980) 325.
- [2] L.M. Petkovic, D.M. Ginosar, H.W. Rollins, K.C. Burch, C. Deiana, H.S. Silva, M.F. Sardella, D. Granados, *Int. J. Hydrogen Energy* 34 (2009) 4057.

- [3] D.M. Ginosar, L.M. Petkovic, K.C. Burch, *Int. J. Hydrogen Energy* 36 (2011) 8908.
- [4] Z.H. Wang, Y. Chen, C. Zhou, R. Whiddon, Y.W. Zhang, J.H. Zhou, K.F. Cen, *Int. J. Hydrogen Energy* 36 (2011) 216.
- [5] X.D. Lin, Y.W. Zhang, R. Wang, Z.H. Wang, J.H. Zhou, K.F. Cen, *Int. J. Hydrogen Energy* 38 (2013) 15003.
- [6] P. Favuzza, C. Felici, L. Nardi, P. Tarquini, A. Tito, *Appl. Catal. B: Environ.* 105 (2011) 30.
- [7] L.J. Wang, Q. Han, D.C. Li, Z.C. Wang, J. Chen, S.Z. Chen, P. Zhang, B.J. Liu, M.F. Wen, J.M. Xu, *Int. J. Hydrogen Energy* 38 (2013) 109.
- [8] J.M. Kim, J.E. Park, Y.H. Kim, K.S. Kang, C.H. Kim, C.S. Park, K.K. Bae, *Int. J. Hydrogen Energy* 33 (2008) 4974.
- [9] K. Dasgupta, D. Sathiyamoorthy, *Mater. Sci. Technol.* 19 (2003) 995.
- [10] N. Shimodaira, A. Masui, *J. Appl. Phys.* 92 (2002) 902.
- [11] I. Velo-Gala, J.J. López-Peñalver, M. Sánchez-Polo, J. Rivera-Utrilla, *Carbon* 67 (2014) 236.
- [12] P.J.F. Harris, *Crit. Rev. Solid State Mater. Sci.* 30 (2005) 235.
- [13] D. Beeman, J. Silverman, R. Lynds, M.R. Anderson, *Phys. Rev. B* 30 (1984) 870.
- [14] N. Larouche, B.L. Stansfield, *Carbon* 48 (2010) 620.
- [15] A. Rey, J.A. Zazo, J.A. Casas, A. Bahamonde, J.J. Rodriguez, *Appl. Catal. A: Gen.* 402 (2011) 146.
- [16] J. Collins, T. Ngo, D. Qu, M. Foster, *Carbon* 57 (2013) 174.
- [17] K. Nakada, M. Fujita, G. Dresselhaus, M.S. Dresselhaus, *Phys. Rev. B* 54 (1996) 17954.
- [18] P. Delhaes, M. Couzi, M. Trinquedelle, J. Dentzer, H. Hamidou, C. Vix-Guterl, *Carbon* 44 (2006) 3005.
- [19] A. Szczygielska, A. Burian, S. Duber, J.C. Dore, V. Honkimaki, *J. Alloys Compd.* 328 (2001) 231.
- [20] J.G. Zhao, L.X. Yang, F.Y. Li, R.C. Yu, C.Q. Jin, *Carbon* 47 (2009) 744.
- [21] M.S. Dresselhaus, A. Jorio, M. Hofmann, G. Dresselhaus, R. Saito, *Nano Lett.* 10 (2010) 751.
- [22] A.C. Ferrari, D.M. Basko, *Nat. Nanotechnol.* 8 (2013) 235.
- [23] L.G. Cancado, A. Jorio, E.H.M. Ferreira, F. Stavale, C.A. Achete, R.B. Capaz, M.V.O. Moutinho, A. Lombardo, T.S. Kulmala, A.C. Ferrari, *Nano Lett.* 11 (2011) 3190.
- [24] Z.-L. Zhang, R. Brydson, Z. Aslam, S. Reddy, A. Brown, A. Westwood, B. Rand, *Carbon* 49 (2011) 5049.
- [25] O.O. Sonibare, T. Haeger, S.F. Foley, *Energy* 35 (2010) 5347.
- [26] C.M. Dominguez, P. Ocon, A. Quintanilla, J.A. Casas, J.J. Rodriguez, *Appl. Catal. B: Environ.* 140 (2013) 663.
- [27] A. Sadezky, H. Muckenhuber, H. Grothe, R. Niessner, U. Pöschl, *Carbon* 43 (2005) 1731.
- [28] Y. Wang, D.C. Alsmeyer, R.L. McCreery, *Chem. Mater.* 2 (1990) 557.
- [29] J.-P. Tessonnier, D. Rosenthal, T.W. Hansen, C. Hess, M.E. Schuster, R. Blume, F. Girgsdies, N. Pfänder, O. Timpe, D.S. Su, R. Schlögl, *Carbon* 47 (2009) 1779.
- [30] E.F. Antunes, A.O. Lobo, E.J. Corat, V.J. Trava-Airoldi, A.A. Martin, C. Verissimo, *Carbon* 44 (2006) 2202.
- [31] A.C. Ferrari, J. Robertson, *Phys. Rev. B* 61 (2000) 14095.
- [32] F. Tuinstra, J.L. Koenig, *J. Compos. Mater.* 4 (1970) 492.
- [33] A.C. Ferrari, *Solid State Commun.* 143 (2007) 47.
- [34] J.L. Figueiredo, M.F.R. Pereira, *Catal. Today* 150 (2010) 2.
- [35] H. Estrade-Szwarczkopf, *Carbon* 42 (2004) 1713.
- [36] M. Frisch, G. Trucks, H. Schlegel, G. Scuseria, M. Robb, J. Cheeseman, J. Montgomery Jr., T. Vreven, K. Kudin, J. Burant, Gaussian 03, Revision D.01, Gaussian, Inc., Wallingford, CT, 2004.
- [37] K. Sendt, B. Haynes, *Combust. Flame* 143 (2005) 629.
- [38] L.R. Radovic, *Carbon* 43 (2005) 907.
- [39] Y.W. Zhang, Z.H. Wang, J.H. Zhou, J.Z. Liu, K.F. Cen, *Int. J. Hydrogen Energy* 33 (2008) 627.
- [40] T.D.B. Nguyen, Y.-K. Cho, W.C. Cho, K.S. Kang, S.U. Jeong, C.H. Kim, C.-S. Park, K.-K. Bae, *Appl. Energy* 115 (2014) 531.
- [41] L. Chen, A.C. Cooper, G.P. Pez, H. Cheng, *J. Phys. Chem. C* 111 (2007) 18995.
- [42] W.H. Harman, T.P. Lin, J.C. Peters, *Angew. Chem. Int. Ed.* 53 (2014) 1081.